NEMA NU 4-2008 and In-Vivo Imaging Performance of RAYCAN Trans-PET/CT X5 Small Animal Imaging System

J. Teuho[1,2], C. Han[1], L. Riehakainen[1], A Honkaniemi[1], M. Tirri[1,6], H. Liljenbäck[1], J. Virta[1], S. Gu[3], S. Liu[4], L. Wan[5], M. Teräs[2,6], A. Roivainen[1], Q. Xie[7] and J. Knuuti[1]

1 Turku PET Centre, University of Turku and Turku University Hospital, Turku, Finland

2 Department of Medical Physics, Division of Medical Imaging, Turku University Hospital, Turku, Finland

3 RAYCAN Technology Co., Ltd, Suzhou, China

4 RaySolution Digital Medical Imaging Co., Ltd, Ezhou, China

5 RayData Technology, Co.,Ltd, Wuhan, China

6 Department of Biomedicine, University of Turku, Turku, Finland

7 Department of Biomedical Engineering, Huazhong University of Science and Technology, Wuhan, China

Abstract

The RAYCAN Trans-PET/CT X5 is a preclinical positron emission tomography and computed tomography (PET/CT) system intended for in-vivo imaging of rats and mice, featuring all-digital readout electronics for PET data acquisition.

The National Electrical Manufacturers Association (NEMA) NU 4-2008 performance evaluation was conducted on the RAYCAN Trans-PET/CT X5 in addition to assessing in-vivo imaging performance of the system on live animals. The performance characteristics of the system were evaluated, including system spatial resolution, count rate performance, sensitivity and image quality. The system imaging performance is assessed in dynamic in-vivo PET imaging.

The system resolution defined as full width half maximum (FWHM) was 2.07 mm, 2.11 mm and 1.31 mm for the tangential, radial and axial resolution, respectively, at the center of the field of view. The peak noise equivalent count rate (NECR) values measured were 61 kcps at 0.19 MBq/mL for the rat size phantom and 126 kcps at 1.53 MBq/mL for the mouse size phantom. Scatter fractions were 24% and 14% for the rat and mouse phantom. The measured peak sensitivity of the system was 1.70 %. Image quality in static imaging was deemed sufficient based on the image quality phantom study, with average activity concentration of 155 ± 8.6 kBq/mL and image uniformity of 5.57% when using two-dimensional filtered backprojection algorithm (2D-FBP). Rods in the image quality phantom were visualized easily up to 2 mm in size. In dynamic in-vivo PET imaging, time-activity-curves from several regions were successfully measured, characterizing the radioactivity distribution in myocardial blood pool, liver, left ventricle and the lung.

In conclusion, the RAYCAN Trans-PET/CT X5 system can be considered a suitable option for basic imaging needs in preclinical imaging.

Keywords: small-animal PET/CT system, performance evaluation, NEMA, preclinical PET imaging

I. INTRODUCTION

Preclinical positron emission tomography / computed tomography (PET/CT) imaging is an essential research tool for disease research and pharmacological development. Preclinical PET allows the study of processes in small animal models related to disease progression, effectiveness of treatments, and development of novel tracers and pharmacological agents (Levin and Zaidi et al 2007). The entire dynamic biodistribution of labeled compounds in the body can be studied, potentially with kinetic analysis and tracer uptake modelling. Imaging of a single subject can be performed multiple times to study disease progression and therapeutic outcomes. Combined with conventional invasive animal study techniques, such as tissue dissection, preclinical PET is a powerful tool for many research applications (Yao et al 2012).

Small animal PET/CT system instrumentation is an active field of research, as from year 1995 to year 2018, several research prototypes (Bloomfield et al 1995, Lecomte et al 1996, Cherry et al 1997, Jeavons et al 1999, Del Guerra et al 1998, Surti et al 2003, Tai et al 2003, Rouze et al 2004, Ziemons et al 2005, Goertzen et al 2012, Gu et al 2013, Sato et al 2016) as well as commercial systems for small animal imaging have been introduced and evaluated (Schafers et al 2005, Tai et al 2005, Wang et al 2006, Huisman et al 2007, Bao et al 2009, Bergeron et al 2009, Prasad et al 2010, Cañadas et al 2011, Szanda et al 2011, Goertzen et al 2012, Spinks et al 2014, Wang et al 2015, Belcari et al 2017, Krishnamoorthy et al 2018). Performance evaluation of different PET systems has become an essential tool in determining how different factors in system hardware and software design affect the overall system performance. Whenever a new system becomes available, it is essential to investigate and compare the PET system performance characteristics in a standardized manner.

The National Electrical Manufacturers Association (NEMA) NU 4-2008 measurements have been designed to allow comparison between imaging systems and measurement of imaging system performance in a standardized manner (NEMA2008). The NEMA NU 4-2008 standard for preclinical imaging describes a series of phantom imaging tests for system sensitivity, spatial resolution, count rate performance and image quality (NEMA 2008). In addition, it is also common practice to evaluate the performance of the system using live animals, as these can be considered to be the final indicator of system performance in-vivo as compared to phantom tests.

The RAYCAN Trans-PET/CT X5 is a commercial small-animal imaging system based on the previously introduced Raycan Trans-PET BioCaliburn LH PET-only system (Wang et al 2015) which includes a CT system for PET attenuation correction and anatomical localization. The RAYCAN Trans-PET/CT X5 is the first preclinical PET/CT system to feature detector technology based on all-digital readout electronics for PET data acquisition (Xie et al 2013) and a multi-voltage threshold (MVT) technique introduced in (Xie et al 2005, Xie et al 2009, Kim et al 2009). The detector configuration consists of basic detector modules (Xie et al 2013), which potentially allow application of novel event-analysis algorithms (Xie et al 2009) and can be conveniently modified to new detector and PET system designs with a low development cost and ease of upgradability (Xie et al 2013).

In this study, we performed the NEMA NU 4-2008 and an in-vivo imaging evaluation for the RAYCAN preclinical Trans-PET/CT X5 system prototype and compared the measurement results to the reported values of the PET-only Trans-PET BioCaliburn LH system (Wang et al 2015). All measurements were performed according to the specification of NEMA NU 4-2008 standard. We report the values measured in the following tests: spatial resolution, sensitivity, count rate performance and image quality. In addition, results of in-vivo dynamic PET imaging with the system are reported. Finally, this is the first paper to report the imaging performance of the RAYCAN preclinical Trans-PET/CT X5 system.

II. MATERIALS AND METHODS

PET and CT system specifications

The RAYCAN Trans-PET/CT X5 system (RAYCAN Technology, Suzhou, China) system specifications summarized in Table 1. The system employs a ring configuration of a dodecagonal shape, offering a transaxial and axial field of view (FOV) of 130 mm and 50 mm, respectively. The system contains 12 block detector modules that are arranged on a 19.2 cm diameter ring configuration, with detector crystal size of 1.9 x 1.9 x 13 mm. The bore size of the system is 160 cm, potentially allowing simultaneous imaging of multiple rodents. Detailed information about the detector design and the digital data acquisition technique applied can be found in (Wang et al 2015).

Parameter	Specification
Detector crystal and dimension (mm)	LYSO, $1.89 \times 1.89 \times 13.00$
Number of detector rings	26
Total number of crystals	8112
Detector ring diameter (cm)	19.2
PET transaxial FOV (mm)	130
PET axial FOV (mm)	53
Energy resolution (%)	15
Energy window (keV)	350 – 650
Coincidence timing window (ns)	5
CT axial FOV (mm)	105
CT resolution (μm)	120

Table 1. Technical specifications of the Trans-PET/CT X5 system. LYSO = lutetium-yttrium oxyorthosilicate, FOV = field of view.

In comparison to the previous PET-only design of Trans-PET BioCaliburn LH, a CT system has been implemented in a single gantry configuration, allowing us to acquire CT images for anatomical localization and PET attenuation correction. According to the manufacturer, slight change to the PET data acquisition system have been made by updating the system firmware and circuitry.

Image reconstruction

The Trans-PET/CT X5 implements two-dimensional filtered backprojection (2D-FBP) algorithm in addition to three-dimensional ordered subset expectation maximization algorithm with point spread function modelling (OSEM3D-PSF) (Kao et al 2009, Liu et al 2014) for PET image reconstruction. The image matrix sizes for 2D-FBP and OSEM3D-PSF are 140×140×47 and 280×280×100 with isotropic voxel sizes of 1.0 mm³ and 0.5 mm³, respectively. For OSEM3D-PSF, the default number of iterations and subsets are 2 and 12, which were not modified during the study. Gaussian image post-filtering can be applied with the following parameters: none, low (window size = 3, sigma =1), normal (window size = 5, sigma =2) and high (window size = 7, sigma = 4).

A system implements corrections for dead-time, decay, normalization, geometric effects and attenuation. Randoms and scatter correction are not implemented. The default energy window and coincidence timing window are set to 350 to 650 keV and 5 ns. Unless otherwise stated, all PET studies described below are acquired with this energy and coincidence timing window. The scanner acquires data in list-mode, rebinning the data to 3D sinograms, which were further rebinned to 2D sinograms with single-slice rebinning (SSRB) as required by the NEMA analysis protocol.

PET and CT system calibrations

The system implements calibrations for detector normalization and well counter correction for the PET system with CT detector calibration and Hounsfield Unit (HU) scale calibration for the CT system. The PET system implements component-based normalization method combined with the maximum-likelihood estimation method proposed by Hogg et al (Hogg et al 2001). A ^{18}F-FDG planar source with a size of 120×90 mm² is used. The normalization data is collected at three rotational positions with an angular interval of 60 degrees,

the first of which is on the x-z plane of the scanner (Wang et al 2015). The recommended dose range for normalization is 11.1 MBq to 14.8 MBq, with an acquisition time of 30 min at each rotational position.

NEMA NU 4-2008 measurements and analysis

We performed the following measurements on the RAYCAN Trans-PET/CT X5 system, as specified by NEMA NU 4-2008: spatial resolution, sensitivity, count rate performance and the image quality evaluations. Live animal imaging performance of the system was assessed by imaging of one rat with ^{18}F-FDG.

The phantoms were imaged as specified by the NEMA NU-4 2008 standard, following the recommended protocol given by manufacturer. All recorded doses were measured with a Veenstra VDC-404 dose calibrator, which was also used to calibrate the imaging system. All measurement data was analyzed as recommended by the NEMA NU-4 2008 standard, with in-house programs developed in MATLAB.

Spatial resolution

The spatial resolution measurement was performed using a ^{22}Na point source embedded in a 1x1x1 cm^3 acrylic cube (Eckert and Ziegler, Valencia, CA). The active diameter of the source was 0.25 mm with an activity of 0.342 MBq at the time of the measurement.

Measurement data were collected in the center of the axial FOV and one fourth of the axial FOV at 12.5 mm offset. The measurements were collected at radial distances of 5 mm, 10 mm, 15 mm, 25 mm and 50 mm from the center of the FOV. Each measurement was collected with a 60 second acquisition time, containing more than the required 10^5 prompt counts. All acquisitions were performed without CT-based attenuation correction. The PET images were reconstructed with 2D-FBP using SSRB for data rebinning. The image matrix and pixel size were 140x140x47 and 1 x 1 mm with a slice thickness of 1 mm. No post-smoothing was applied.

The spatial resolution was determined by calculating the full width at half maximum and tenth maximum (FWHM and FWTM) of the point source response functions in radial, tangential and axial directions. We refer to NEMA guideline section 3.4 for full details of the calculation (NEMA 2008). In short, the response functions were formed by summing one-dimensional profiles parallel to the direction of the measurement. Thereafter, the maximum value of the response function was determined from the peak of the response function. Finally, FWHM and FWTM were determined by linear interpolation between adjacent pixels, followed by conversion from pixels to millimeters. We report the radial, tangential and axial resolution FWHM and FWTM for each radial offset.

System count-rate performance

The count rate performance of the system was studied by imaging a rat-size and mouse-size cylindrical phantoms constructed from polyethylene with a specified density of 0.96 g/cm^3 and a line source insert, with injectable volumes measured as 0.22 mL for the rat phantom 0.11 mL for the mouse phantom. The phantoms were constructed in-house according to the dimensions and specifications of the NEMA standard (NEMA 2008).

The rat size phantom was injected with 123.71 MBq of ^{18}F-FDG while the mouse size phantom was injected with 106.54 MBq of ^{18}F-FDG. The imaging of the rat phantom started 10 minutes from injection while the imaging of the mouse phantom started 6 minutes from injection. Measurements were performed until the activity in the phantom had decayed under two times the intrinsic background rate of 106 cps. Individual image acquisitions were 5 minutes in length. During the first hour of scanning, acquisitions were repeated every 7 minutes, leaving 2 minutes between scans. During the 2nd hour, acquisitions were repeated every 10 minutes. During 2 to 5 hours, acquisitions were repeated every 25 minutes. After 5 hours, the image acquisitions were repeated every 35 minutes. The total duration of the count-rate measurements was 14 hours 21 minutes for the rat phantom and 14 hours 17 minutes for the mouse phantom. A background measurement with 5 minute duration was collected to estimate the intrinsic background rate.

Analysis of the count rate measurements

The sinogram data was extracted from the system. All of the data extracted contained the total acquired counts without corrections. Oblique sinograms were collapsed into single sinograms for each respective slice by using SSRB. The SSRB sinogram data was analyzed and processed as follows. First, all of the pixels farther than 8 mm from the edges of the phantom were set to zero. Thereafter, all of the data were centered in the projection space. The centering was performed for each projection by first finding the pixel with the largest value and then shifting the projection so that the maximum value is aligned with the central pixel of the sinogram. After alignment of all projections, a sum projection was produced as the sum of pixels in each angular projection

The counts $C_{L,i,j}$ and $C_{R,i,j}$ were obtained from the sum projection as defined in the NEMA guideline section 4.4, Figure 4.2 (NEMA 2008). Specifically, counts $C_{L,i,j}$ and $C_{R,i,j}$ refer to left and right pixel intensities at the edges of a 14 mm wide strip at the center of the sum projection. Linear interpolation was applied to find the pixel intensities $C_{L,i,j}$ and $C_{R,i,j}$ at +-7 mm from the central pixel of the sum projection as specified in the NEMA NU-4 2008 standard. The average of these pixel intensities was multiplied by the value of pixels between the edges of the 14 mm wide strip and the product was added to the counts in the pixels outside the strip, to estimate the number of random plus scattered events $C_{randoms+scatter,i,j}$ for slice i of the acquisition j. The total event count $C_{total,i,j}$ was defined as the sum of all pixels in the sum projection for slice i of acquisition j. Thereafter, the average activity in MBq/mL in each acquisition was calculated as described by NEMA standard Section 1.2 (NEMA 2008).

The following parameters were calculated from the sinogram data: total event rate, true event rate, random event rate, scattered event rate and noise equivalent count rate in addition to evaluation of scatter fraction and total system scatter fraction.

The total event rate $R_{total,i,j}$ was evaluated as:

$$R_{total,i,j=} C_{total,i,j}/T_{acq,j} \tag{1}$$

where $C_{total,i,j}$ is the total event count divided by acquisition time $T_{acq,j}$ of each individual acquisition. The system total event rate $R_{total,j}$ is calculated as a sum of $R_{total,i,j}$ over all slices i.

The true event rate $R_{true,i,j}$ was calculated as:

$$R_{true,i,j=}(C_{total,i,j} - C_{randoms+scatter,i,j})/T_{acq,j}, \tag{2}$$

where the system true event rate $R_{true,j}$ is calculated as sum of $R_{true,i,j}$ over all slices i.

As the RAYCAN system does not estimate random coincidences, the random event rate $R_{random,i,j}$ was calculated as:

$$R_{random,i,j=} R_{total,i,j} - (R_{true,i,j}/[1 - SF_i]), \tag{3}$$

, where the system random event rate $R_{random,j}$ is calculated as sum of $R_{random,i,j}$ over all slices i and SF_i is the scatter fraction from final acquisitions j', with count loss and random event rates below 1 % in both the rat and mouse phantom examinations, calculated as:

$$SF_{i=}\sum_{j'} C_{randoms+scatter,i,j'}/\sum_{j'} C_{total,i,j'}. \tag{4}$$

The scattered event rate $R_{scatter,i,j}$ was evaluated for each slice as:

$$R_{scatter,i,j=}R_{total,i,j} - R_{true,i,j} - R_{random,i,j} - R_{int,i,j}, \tag{5}$$

where $R_{int,i,j}$ is the intrinsic background count rate from the background measurement. The system scattered event rate $R_{scatter,j}$ is calculated as sum of $R_{scatter,i,j}$ over all slices i.

The system scatter fraction SF_j for each acquisition j was calculated as the ratio of scattered event rate to the sum of true and scattered event rates for a system with intrinsic radioactivity as:

$$SF_{j=} R_{scatter,j}/(R_{true,j} + R_{scatter,j}), \tag{6}$$

and the total system scatter fraction SF_{tot} was evaluated by summing over the final acquisitions j', where count loss and random event rates were determined to be below 1 %.

Finally, the noise equivalent count rate (NECR) $R_{NEC,i,j}$ was calculated for each slice as:

$$R_{NEC,i,j=} R_{true,i,j}^2/R_{total,i,j} \tag{7}$$

The NECR $R_{NEC,j}$ was calculated as sum of $R_{NEC,i,j}$ over all slices i.

We report the system true $R_{true,j}$, random $R_{random,j}$, scattered $R_{scatter,j}$, total $R_{total,j}$ event rates and NECR $R_{NEC,j}$ as a function of average activity concentration, calculated from the injected activity and the total volume of the phantom (294.52 mL for the rat phantom and 34.36 mL for the mouse phantom). In addition, we report the peak true count rate, peak NECR, system total scatter fraction SF_{tot} and the corresponding activity concentrations.

System sensitivity

The sensitivity measurement was performed using the same ^{22}Na point source as with the spatial resolution measurement. The activity of the source was recorded as 0.340 MBq at the time of the acquisition (A_{cal}). The source was imaged as proposed by the standard, with the exception of using a stepping size of 0.5 mm. The intrinsic sinogram plane thickness is 0.586 mm as opposed to the slice thickness of 1 mm used in the FBP reconstruction. The acquisition time for each step was 60 seconds.

The source was placed in the center of the scanner FOV and then moved in 0.5 mm steps by moving the bed to the next source location by system control software. After the measurements to one direction were collected, another set of measurements was collected in the opposite direction of the axial FOV. In total, 101 points were collected. The respective background rate was collected by acquiring background counts for 60 seconds with the absence of the source.

Analysis of the sensitivity measurements

For the sensitivity measurement, both the phantom and background sinograms were masked by applying a static mask to a 20 mm region from the center of the sinogram. As opposite of finding the maximum value in the sinogram automatically for all angles, we applied a static mask as we noticed that automatic detection of the maximum value may not be reliable for all of the angles in the outermost slices due increase of noise.

The total counts in each sinogram were then summed to form the total counts for each slice, respectively. The counting rate R_i was then determined by dividing the masked sinogram sum by the acquisition time T_{acq}. Applying the same mask for the background acquisition and dividing the sinogram sum by the acquisition time was used to calculate the background count rate $R_{B,i}$.

The sensitivity S_i (cps/Bq) and the absolute sensitivity $S_{A,i}$ (%) for each slice i were calculated from equations 8 and 9, as:

$$S_{i=}(R_i - R_{B,i})/A_{cal} \tag{8}$$

and

$$S_{A,i=} S_i/0.9060 \times 100 \%, \tag{9}$$

where 0.9060 is the branching ratio of ^{22}Na.

As the system has an FOV size smaller than 7 cm, we calculated only the total system sensitivities S_{tot} and $S_{A,tot}$. The total sensitivities are calculated as an average over all slices, by summation of the sensitivities from equations 8 and 9 followed by division with the number of slices N, as stated by the standard. The equations used for calculation of total system sensitivities are defined as:

$$S_{tot=}\frac{1}{N}\sum_{i}^{all} S_i \qquad (10)$$

and

$$S_{A,tot=}\frac{1}{N}\sum_{i}^{all} S_{A,i}, \qquad (11)$$

where N equals the number of slices, 101 in total. In addition to total sensitivity S_{tot} (cps/Bq) and the total absolute sensitivity $S_{A,tot}$ (%), we also report the peak absolute sensitivity.

Image quality phantom measurements

The visual image quality and recovery coefficients were studied by measuring the NEMA Image Quality phantom with 3.62 MBq activity of ^{18}F-FDG. The total volume of the phantom was measured to be 22 mL. The image acquisition duration was set to 20 minutes. A CT scan using the standard protocol for attenuation correction was applied.

For PET image reconstruction, both 2D-FBP and OSEM3D-PSF were used. The image matrix sizes for 2D-FBP and OSEM3D-PSF were 140×140×47 and 280×280×100 with isotropic voxel sizes of 1.0 mm^3 and 0.5 mm^3, respectively. The default number of iterations (2) and subsets (12) were used for the OSEM3D-PSF reconstruction. The PET images were reconstructed with all available corrections, including detector normalization, dead-time and attenuation. Images were reconstructed with low post-smoothing values using a Gaussian filter with window width of 3 pixels and sigma of 1 pixel.

Image quality phantom analysis

The image quality phantom data was analyzed in terms of image uniformity, recovery coefficients (%RC) and accuracy of data corrections. Uniformity was measured by drawing a 22.5 mm diameter and 10 mm long cylindrical volume of interest (VOI) over the center of the uniform region of the image quality phantom. The average activity concentration in kBq/mL with the minimum, maximum and percentage standard deviation were measured.

The %RC were calculated as described in the NEMA standard. The image slices over the central 10 mm length of the rods were averaged to obtain one average slice of the rods. Circular regions of interest (ROIs) were drawn around each rod with diameters of twice the size of the physical diameter of the rods. From the ROIs, the maximum values were measured and the location of the maximum pixel coordinates was determined. The pixel coordinates were then used to create line profiles along the rods in the axial direction.

To calculate the %RC, the mean pixel values in each rod were divided by the mean activity measured from the uniform region to determine the %RC for each rod. Thereafter, the percent standard deviation (%STD_{RC}) of the recovery coefficients for each rod was determined from equation 12, as stated by the standard:

$$\%STD_{RC=}100\times\sqrt{(STD_{lineprofile}/Mean_{lineprofile})^2 + (STD_{background}/Mean_{background})^2}, \qquad (12)$$

where the mean and standard deviation were calculated from individual line profiles ($Mean_{lineprofile}$ and $STD_{lineprofile}$) and the uninform region of the phantom ($Mean_{background}$ and $STD_{background}$).

The accuracy of corrections was defined by measuring the spill-over of activity in the water and air-filled cylindrical inserts. VOIs of 4 mm in diameter and 7.5 mm length were drawn over the cylindrical inserts. The spill-over-ratio (SOR) was calculated as the ratio of the mean of each cold region to the mean of the uniform region. The standard deviation %STD was calculated in the same manner as the recovery coefficients in equation 12, from the standard deviation and the mean calculated from the cold regions and the uniform region.

In-vivo PET imaging

All data presented in this section have been obtained in animal experiments. All animal experiments were approved by the national Animal Experiment Board in Finland and the Regional State Administrative Agency for Southern Finland (License number, ESAVI/10946/04.10.07/2016) and were conducted in accordance with the relevant European Union directive, implementation of the 2010/63/EU. All animals were handled by qualified personnel.

A single male rat of the BDIX strain (Charles River Laboratories, USA) with turpentine-induced inflammation (Yamada et al 1995) in the right arm was imaged on the system. Isoflurane anaesthesia at 4-5% concentration for induction and 1-2% concentration for maintenance was used. The animal was 7 weeks old, weighed 184 g and was injected with 11.39 MBq of ^{18}F-FDG via a tail vein cannula. A CT scan (1 mA, 50 kVp) was performed before injection for attenuation correction and anatomical localization, with a duration of 6 minutes using the standard protocol. The CT reconstruction was performed with the standard reconstruction parameters, using a normal filter and a Feldkamp, Davis, and Kress (FDK) filtered-backprojection algorithm. The reconstructed voxel size was 0.195 mm with a matrix size of 512x512.

A dynamic PET scan was started immediately from injection with a total duration of 60 minutes. The PET data were acquired over one bed position centered over the region of the heart. Images were reconstructed using the OSEM3D-PSF reconstruction (2 iterations, 12 subsets) using the same reconstruction parameters as were used in the NEMA image quality phantom study, with the exception of using post-smoothing values set to normal. The dynamic PET images were reconstructed with the frame times of 6 x 10 s, 4 x 60 s, 5 x 300 s and 3 x 600 s.

In the PET image analysis, ROIs were drawn on the heart left ventricle cavity, myocardium, muscle, inflammation area and lung area from which time-activity-curves (TACs) were extracted. The uptake in kBq/mL was plotted as a function of time to inspect the accuracy of TACs from injection. Finally, the late time point frames were fused on CT images and the animal images were inspected visually.

III.   **RESULTS**

<u>Spatial resolution</u>

The measured resolution in radial, tangential and axial directions are plotted in Figure 1. In terms of measured FWHM, axial resolution shows the highest uniformity and resolution across the FOV, while radial resolution shows the worst uniformity and resolution. In terms of FWTM, the results are similar, although more variation across different offsets are detected. Resolution uniformity starts to degrade after 15 mm offset, in both FWHM and FWTM. The measured resolution values for FWHM were 2.07 mm, 2.11 mm and 1.31 mm for the tangential, radial and axial resolution at center of FOV. At ¼ of FOV, the corresponding values were 2.36 mm, 2.59 mm and 1.35 mm for the tangential, radial and axial resolution, respectively.
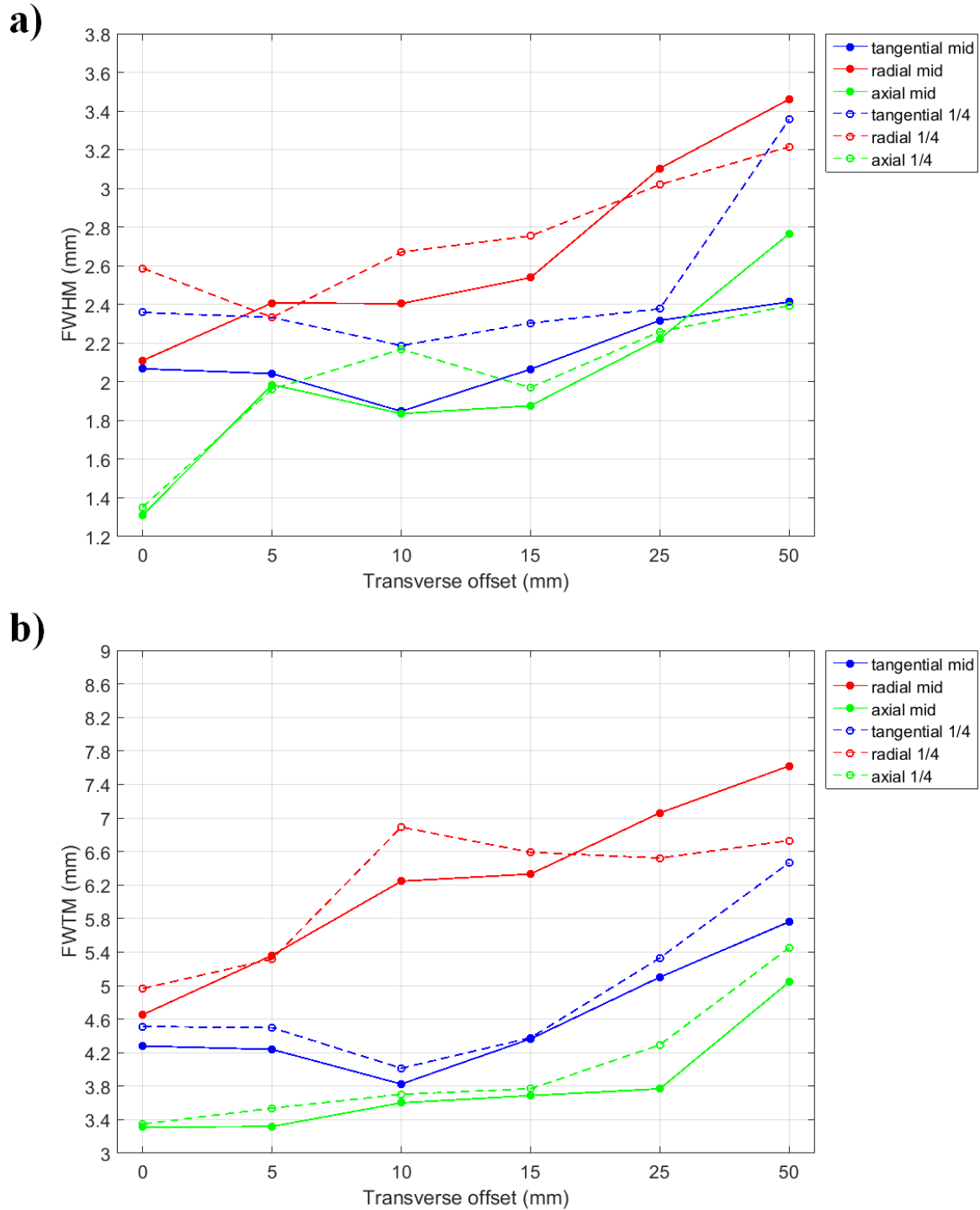
Figure 1. The FWHM (a) and the FWTM (b) plotted as the function of the transverse offset, measured in the center of the axial FOV and at 1/4 offset.

Count-rate performance

The system count rate plot is shown in Figure 2. The system true $R_{true,j}$, random $R_{rndom,j}$, scattered $R_{scatter,j}$, total $R_{total,j}$ event rates and NECR $R_{NEC,j}$ are plotted as a function of activity concentration. The peak trues and NECR were 136 kcps and 126 kcps for the mouse phantom at 1.53 MBq/mL. For the rat phantom, the peak trues and NECR were 70 kcps and 61 kcps at 0.19 MBq/mL. The system total scatter fractions SF_{tot} were 14% and 24% for the mouse and the rat phantom, respectively.
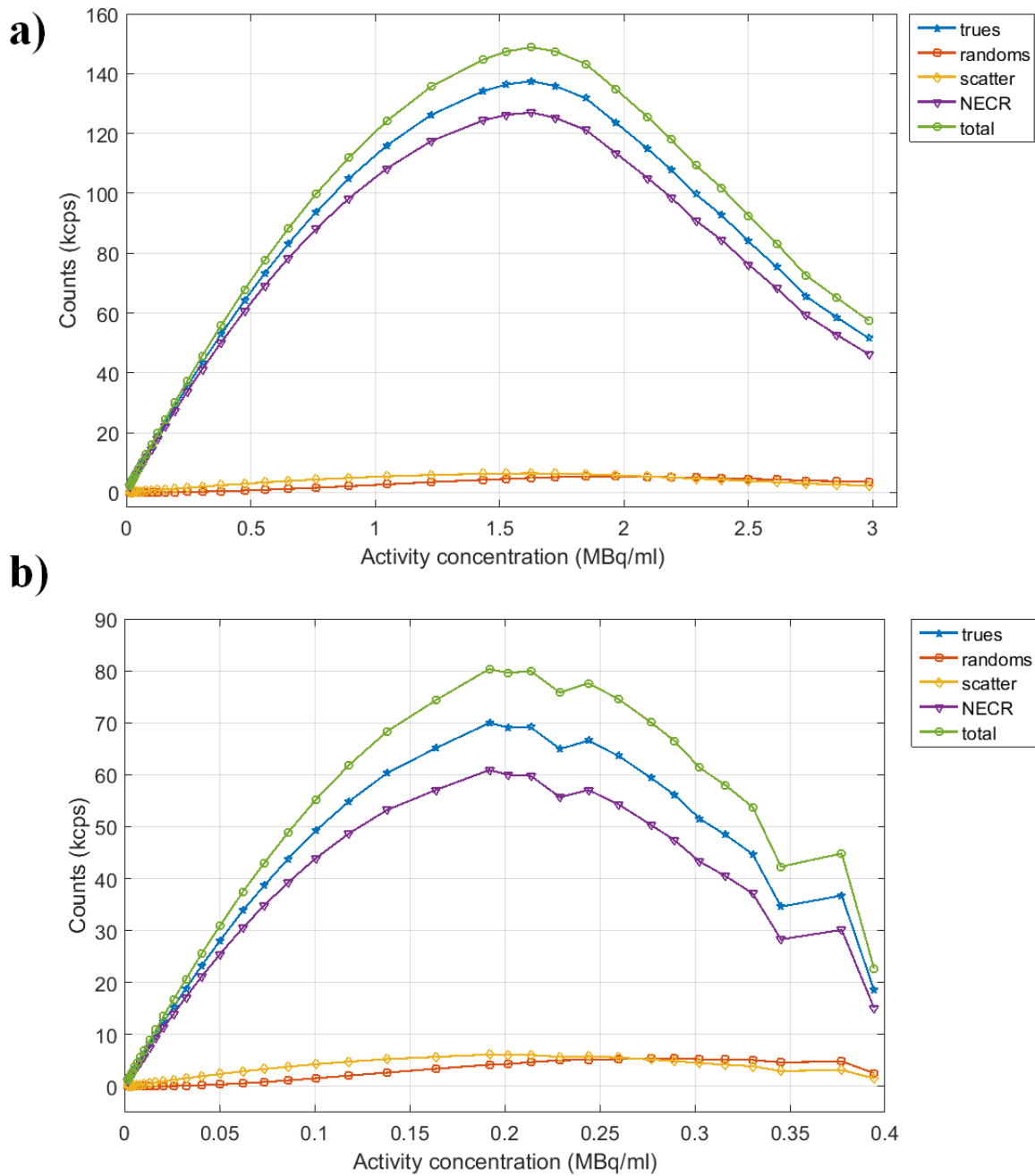
Figure 2. Count-rate curves for the mouse (a) and rat (b) phantom as a function of average activity concentration.

Sensitivity

The results from the sensitivity measurements are summarized in Figure 3. The total system sensitivity S_{tot} was 0.0077 cps/Bq while the total absolute system sensitivity $S_{A,tot}$ was 0.84 %. The peak system sensitivity was 1.70 % at axial offset of 0 mm.
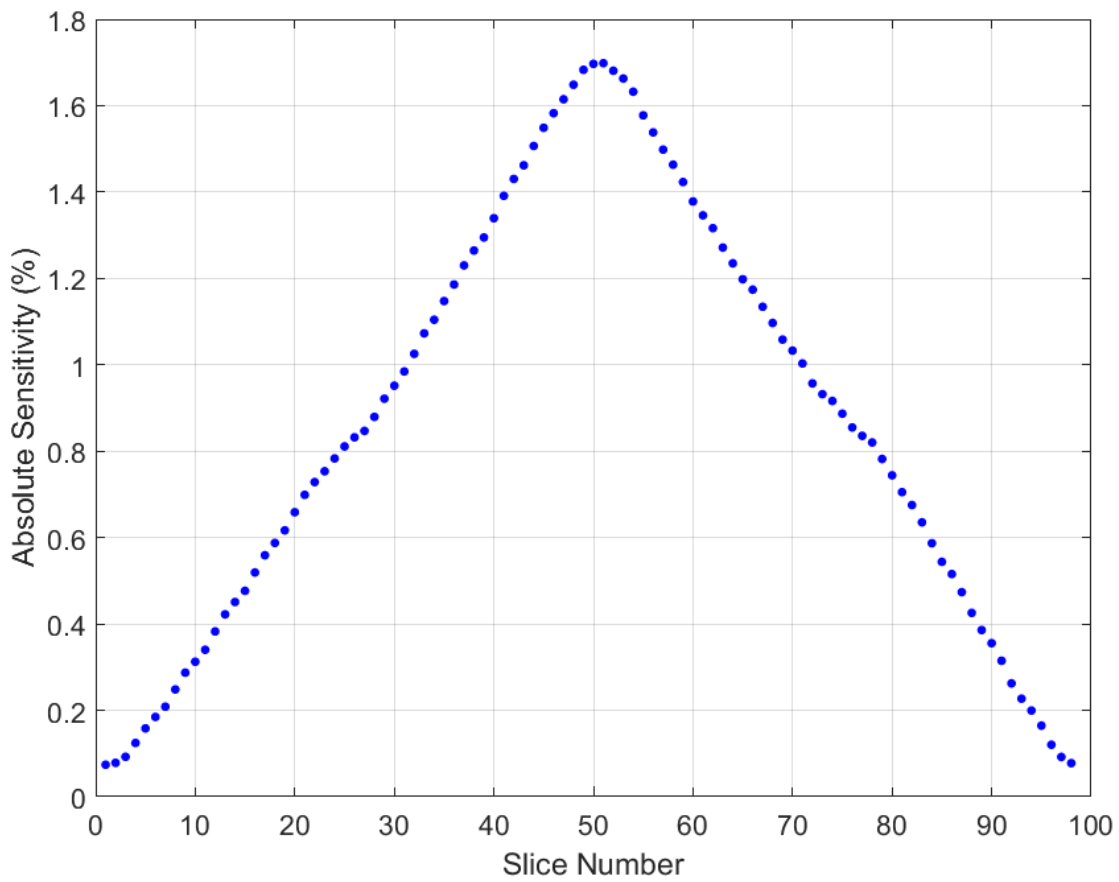
Figure 3. Axial sensitivity profile showing the absolute sensitivity of the system for each measured slice in the axial direction.

Image quality

The %RC and $\%STD_{RC}$ results from the image quality phantom measurements are shown in Figure 4. Image of the rod, air and water compartment and the uniform section of the image quality phantom can be found in Figure 5.

A mean and standard deviation uniformity of 155 ± 8.6 kBq/mL and 157 ± 6.9 kBq/mL were measured with the 2D-FBP and OSEM3D-PSF algorithms. The maximum and minimum values were 187 kBq/mL and 100 kBq/mL for 2D-FBP and 182 kBq/mL and 137 kBq/mL for OSEM3D-PSF. The %STD were measured as 5.57% and 4.36% for the 2D-FBP and OSEM3D-PSF, respectively.

The SOR for the air and water compartment were 7.92% and 17.5% for 2D-FBP and 13.5% and 23.0% for OSEM3D-PSF. The corresponding %STD values for the water and air compartment were 31.4% and 14.7% for 2D-FBP and 12.6% and 12.8% for OSEM3D-PSF.
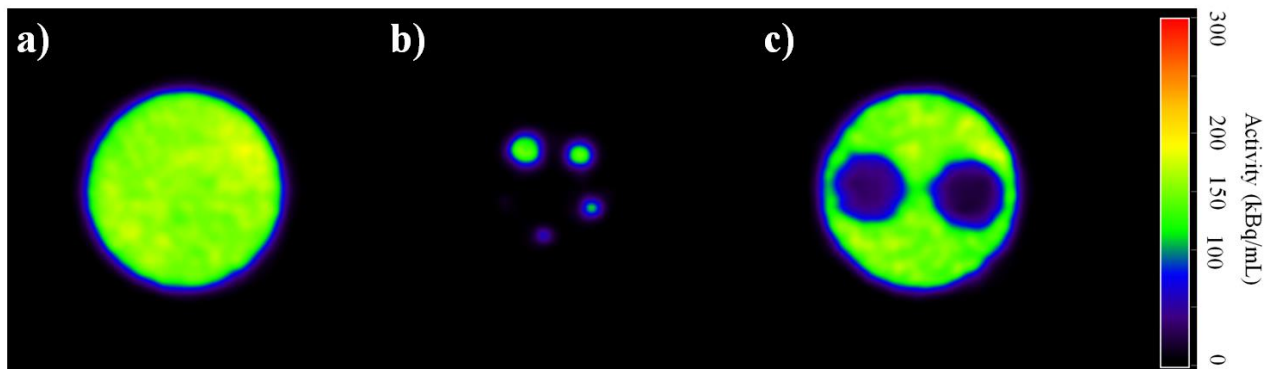
a)
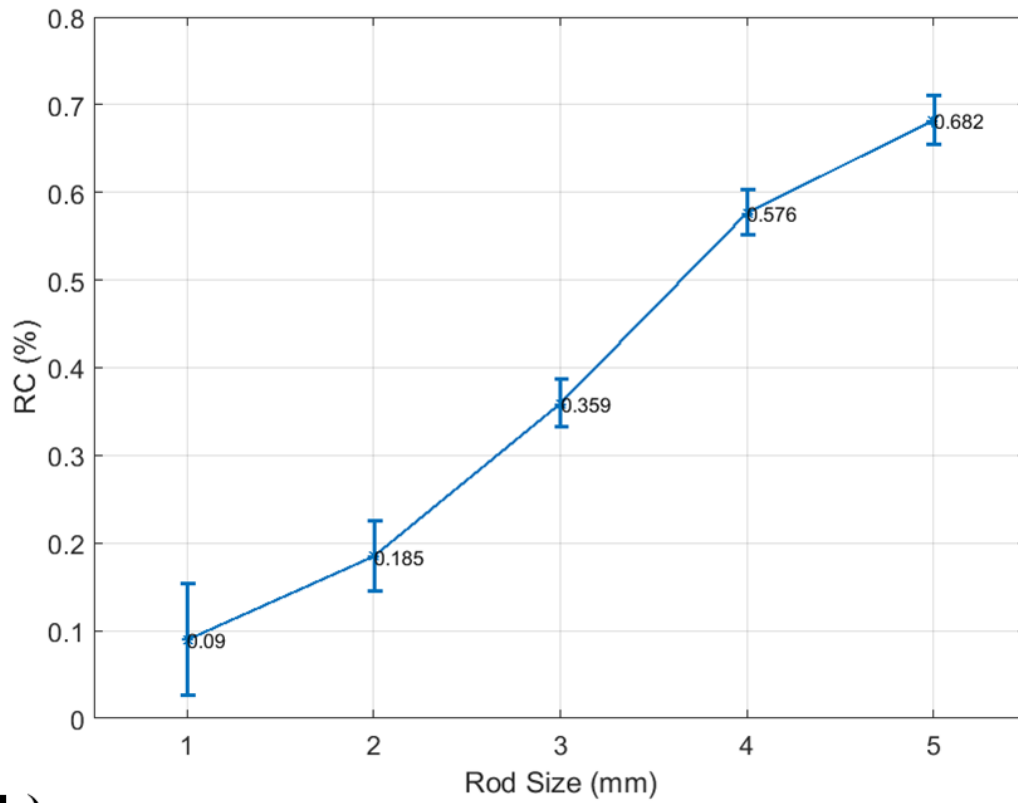
b)
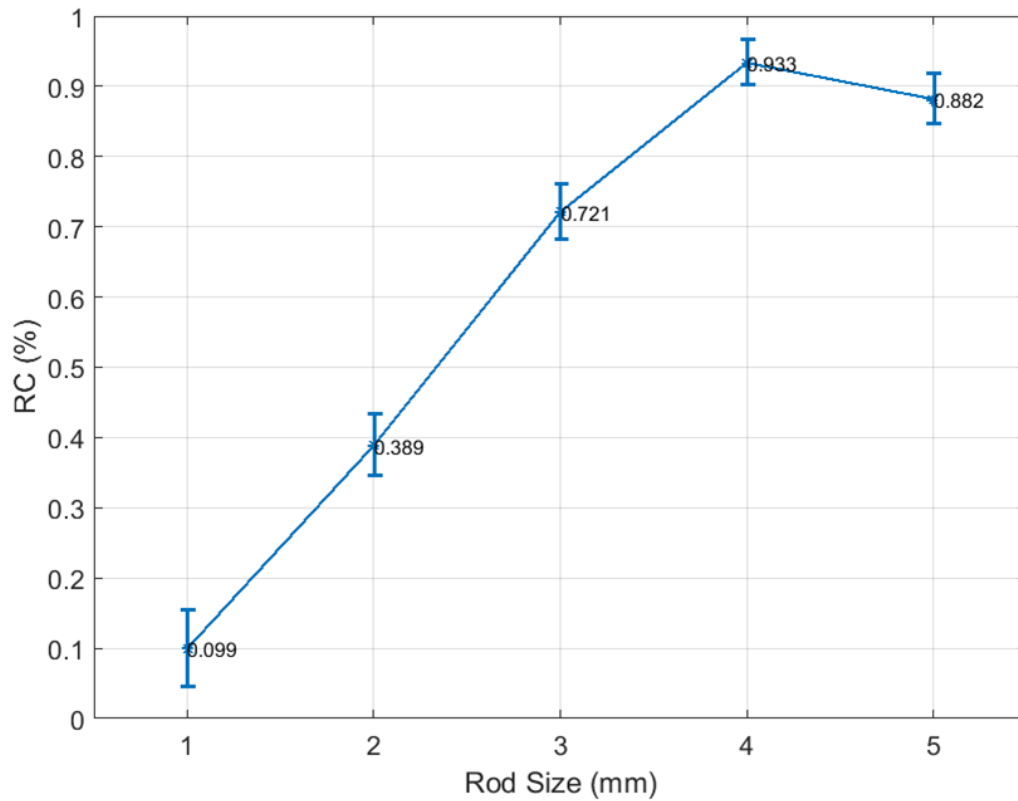
Figure 4. Recovery coefficients (%RC) and %STD from the NEMA image quality phantom measured from 2D-FBP (a) and OSEM3D-PSF (b) reconstructed images.

Figure 5. Images from the NEMA image quality phantom from the uniform (a), rod region (b) and water/air cylinder region (c) with OSEM3D-PSF. The 1 mm size rod is barely differentiable while rods from 2 mm to 5 mm can be easily identified.

In-vivo imaging

The fused CT and PET images from late time frames are shown in Figure 6. Tissue TACs extracted from the anatomical VOI drawn in dynamic PET images are shown in Figure 7. The system shows good image quality in late-time frame ^{18}F-FDG imaging. The induced inflammation can be visually differentiated from the PET images and quantitatively from dynamic TACs. The dynamic TACs derived from each region show a typical radioactivity accumulation expected for each anatomical region.
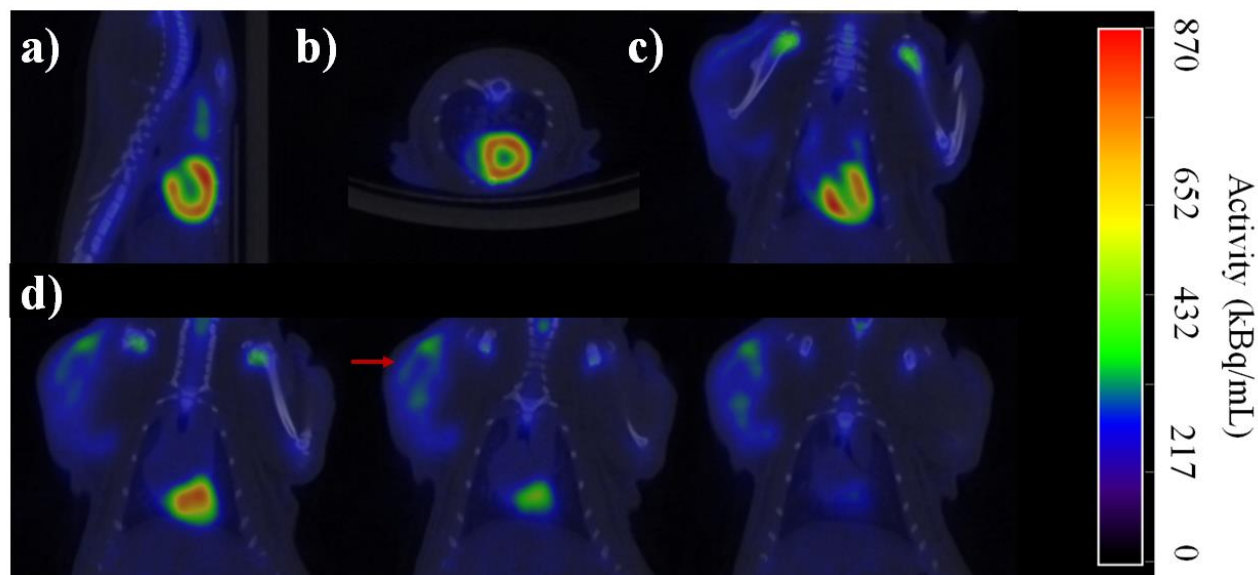
Figure 6. Fused CT and PET images from a rat injected with ^{18}F-FDG and imaged on the Raycan Trans-PET/CT X5 system. Images are shown from the sagittal (a), axial (b) and coronal (c) slices and over the region of the inflammation in (d). The PET images are a sum of the last two dynamic frames with fusion over the anatomical CT scan. The inflammation can be visualized in a PET image shown in (d), differentiated by a red arrow.
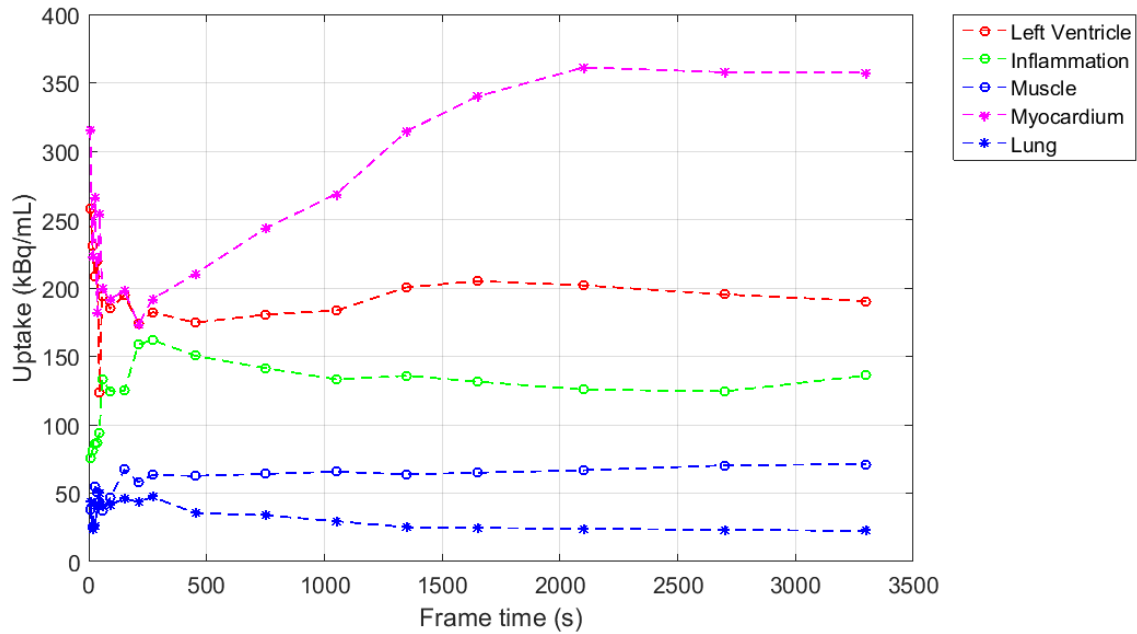
Figure 7. TACs from dynamic PET imaging of the rat. The time points in the plot correspond to uptake measured at mid-frame times, showing typical accumulation expected for ^{18}F-FDG.

IV.   DISCUSSION

The results reported in this study establish a baseline of the performance of the RAYCAN Trans-PET/CT X5 prototype system using the NEMA NU4- 2008 standard. The RAYCAN system shows decent performance capabilities despite the small FOV size in the current configuration. The measurements indicate that the system performance and image quality are sufficient for basic preclinical imaging applications in both static and dynamic PET. The RAYCAN Trans-PET/CT X5 can be considered to be the first commercial preclinical PET/CT system that features all-digital readout electronics and applies the MVT method in data acquisition (Xie et al 2005, Xie et al 2009, Kim et al 2009). Another unique feature of the system is use of the detector module technology described in (Xie et al 2013).

In comparison to Trans-PET BioCaliburn LH in (Wang et al 2015), the Raycan Trans-PET/CT X5 achieves similar performance to the PET-only system, with few exceptions. As the paper of (Wang et al 2015) does not contain the resolution measurements reconstructed with 2D-FBP and does not include FWTM measurements, the results in this paper cannot be compared entirely. However, a similar degradation of the radial resolution can be seen in our measurement results compared to paper of (Wang et al 2015). For direct comparison, we reconstructed our resolution measurements with OSEM3D-PSF (Supplementary Figure 1) and found that they are essentially the same as in (Wang et al 2015). Using OSEM3D-PSF also effectively minimizes the resolution non-uniformity across the FOV.

The most notable differences between systems can be found in count-rate measurements acquired with a 350 keV to 650 keV energy window. The Trans-PET/CT X5 has a peak NECR at 126 kcps at 1.53 MBq/mL for the mouse phantom and 61 kcps at 0.19 MBq/mL for the rat phantom compared to the values of 62 kcps at 0.81 MBq/mL and 25 kcps at 0.11 MBq/mL (Wang et al 2015). The Trans-PET/CT X5 also has a slightly higher scatter fractions for the mouse (14 %) and rat (24 %) phantom versus 8.4% and 17.7% reported in (Wang et al 2015), possibly due to modified gantry design.

Compared to the previous system, the Trans-PET/CT X5 includes additional optimizations in firmware and circuitry, as stated by the system manufacturer. These include an optimized data processing flow and a data buffer set in the detector. In addition, the signal lines on the printed circuit board have been re-arranged. With these optimizations in place, the Trans-PET/CT X5 has been able to overcome the NECR limitations reported for the previous PET-only system in (Wang et al 2015).

Concerning system sensitivity, we measured slightly lower system sensitivity of 1.70 % in Trans-PET/CT X5 compared to value of 2.04% measured in Trans-PET LH (Wang et al 2015). We found no other explanation other than that the sensitivity values in Wang et al (Wang et al 2015) could have been calculated based on the original 3D Michelogram format, omitting rebinning with SSRB and sinogram masking. If the system sensitivity was calculated from the original Michelogram data without SSRB and sinogram masking, we could reproduce a peak sensitivity value of 2.19% (Supplementary Figure 2), close to the value reported by Wang et al (Wang et al 2015). Therefore, it seems that both the Trans-PET LH and Trans-PET/CT X5 have similar performance in terms of system sensitivity.

For the image quality measurements, the image uniformity and recovery coefficients measured with OSEM3D-PSF are very similar between Trans-PET/CT X5 and Trans-PET LH (Wang et al 2105). The spill-over ratios compared to the previous design are slightly higher in Trans-PET/CT X5, which we assume is mostly due to effect of increased scatter due to gantry design. It should be noted that the Trans-PET LH did not include attenuation correction (Wang et al 2015), which might be a contributing factor for the differences detected in the image quality measurements. The relatively large SORs are also explained by missing data corrections for randoms and scatter. In visual image quality assessment, the RAYCAN image quality was deemed to produce PET images of good visual quality and accurately differentiate the radioactivity in different regions.

In comparison to other preclinical imaging systems (Supplementary Table 1), the performance measurements indicate that the system shows PET imaging performance comparable with similar preclinical positron emission tomographs with small axial FOV sizes (Goertzen et al 2012, Riehakainen et al 2018). In terms of raw performance values, the Trans-PET/CT X5 shows resolution properties similar to microPET P4 and R4 series, comparable sensitivity to systems with larger axial FOV (e.g. microPET P4, LabPET8), count-rate performance superior to systems with a maximum axial FOV of 5 cm and similar image quality to most systems (Supplementary Table 1). The Trans-PET/CT X5 can be considered to be quite close to the LabPET8 system (Prasad et al 2011) in most of the performance aspects, although LabPET8 has the advantage in achieving slightly higher count-rate performance and resolution. Overall, the RAYCAN system shows decent imaging capabilities.

The most limiting factor with the current system design is the small axial FOV size of 5 cm. The immediate benefit of an enlarged axial FOV would be increased sensitivity and the ability to cover a wider anatomical region for PET imaging. Previously, an evaluation of three LabPET systems with different FOV sizes has shown that with similar hardware and software configurations, increased axial FOV size results in evident sensitivity gains with reported sensitivities of 1.4%, 2.6%, 4.3% for 4 cm, 8 cm and 12 cm configurations (Bergeron et al 2014). In addition, NEMA performance studies with very recent large FOV systems as the Molecubes (Krishnamoorthy et al 2018) or the IRIS (Belcari et al 2017) have reported system sensitivity values up to 12.4% and 8.0%, respectively.

Finally, it should be noted that the Trans-PET/CT X5 system evaluated in this study was a prototype system which does not include all the necessary quantitative corrections, mainly randoms and scatter. Implementing these data corrections should improve the image quality and quantitative accuracy of the system further. Despite the missing corrections, the PET images obtained from the system are of fairly good quality. According to the manufacturer, further improvements will be included in the system to improve reconstruction protocols and data corrections in addition to moving to a multi-ring configuration, which should bring further increases in system sensitivity. Implementation of these modifications would bring a major performance benefit compared to the current model.

V. CONCLUSIONS

The performance of RAYCAN Trans-PET/CT X5 was characterized using the NEMA NU-4 2008 standard. The system shows similar physical performance to the PET-only Trans-PET BioCaliburn LH system. The performance analysis and in-vivo measurements suggest that the RAYCAN Trans-PET/CT X5 is a suitable option for basic imaging needs in preclinical imaging.

REFERENCES

Bao Q, Newport D, Chen M, Stout D B and Chatziioannou A F 2009 Performance evaluation of the Inveon dedicated PET preclinical tomograph based on the NEMA NU-4 standards J. Nucl. Med. 50 401–8

Belcari N, Camarlinghi N, Ferretti S, Iozzo P, Panetta D, Salvadori P A, Sportelli G, Guerra A D 2017 NEMA NU-4 Performance Evaluation of the IRIS PET/CT Preclinical Scanner. IEEE Transactions on Radiation and Plasma Medical Sciences 1 301–309

Bergeron M et al 2009 Performance evaluation of the LabPET APD-based digital PET scanner IEEE Trans. Nucl. Sci. 56 10–6

Bergeron M, Cadorette J, Tétrault M A, Beaudoin J F, Leroux J D, Fontaine R, Lecomte R 2014 Imaging performance of LabPET APD-based digital PET scanners for pre-clinical research Phys. Med. Biol. 59 661

Bloomfield P M et al 1995 The design and physical characteristics of a small animal positron emission tomograph Phys. Med. Biol. 40 1105–26

Cañadas M, Embid M, Lage E, Desco M, Vaquero J J, Pérez J M 2011 NEMA NU 4-2008 Performance Measurements of Two Commercial Small-Animal PET Scanners: ClearPET and rPET-1. IEEE Trans. Nucl. Sci. 58 58-65

Cherry S R, Shao Y, Silverman R W and Meadors K 1997 MicroPET: a high resolution PET scanner for imaging small animals IEEE Trans. Nucl. Sci. 44 1161–6

Del Guerra A, Di Domenico G, Scandola M and Zavattini G 1998 YAP-PET: first results of a small animal positron emission tomograph based on YAP:Ce finger crystals IEEE Trans. Nucl. Sci. 45 3105

Gu Z, Taschereau R, Vu N T, Wang H, Prout D L, Silverman R W, Bai B, Stout D B, Phelps M E and Chatziioannou A F 2013 NEMA NU-4 performance evaluation of PETbox4, a high sensitivity dedicated PET preclinical tomograph Phys Med Biol. 58 3791-3814

Goertzen A L et al 2012 NEMA NU 4-2008 comparison of preclinical PET imaging systems. J. Nucl. Med. 53 1300–1309

Huisman M C, Reder S, Weber A W, Ziegler S I and Schwaiger M 2007 Performance evaluation of the Philips MOSAIC small animal PET scanner Eur. J. Nucl. Med. Mol. Imaging 34 532–40

Kim H, Kao C M, Xie Q, Chen C T, Zhou L, Tang F, Frisch H, Moses W W, Choong W S 2009 A Multi-Threshold Sampling Method for TOF PET Signal Processing. Nucl. Instrum. Methods Phys. Res. A 602

Krishnamoorthy S, Blankemeyer E, Mollet P, Surti S, Holen R V, Karp J S, 2018. Performance evaluation of the MOLECUBES β -CUBE—a high spatial resolution and high sensitivity small animal PET scanner utilizing monolithic LYSO scintillation detectors. Phys. Med. Biol. 63 155013

Jeavons A P, Chandler R A and Dettmar C A R 1999 A 3D HIDAC-PET camera with sub-millimetre resolution for imaging small animals IEEE Trans. Nucl. Sci. 46 468–73

Lecomte R, Cadorette J, Rodrigue S, Lapointe D, Rouleau D, Bentourkia M, Yao R and Msaki P 1996 Initial results from the Sherbrooke avalanche photodiode positron tomograph IEEE Trans. Nucl. Sci. 43 1952–7

Levin C S and Zaidi H 2007 Current trends in preclinical PET system design Pet. Clin. 2 125–60

Liu J J, Kao C M, Gu S G, Xiao P and Xie Q G 2014 A PET system design by using mixed detectors: resolution properties Phys. Med. Biol. 59 3517–32

National Electrical Manufacturers Association 2008 NEMA standards publication NU 4–2008 Performance Measurements of Small Animal Positron Emission Tomographs (Rosslyn, VA: National Electrical Manufacturers Association)

Prasad R, Ratib O and Zaidi H 2010 Performance evaluation of the FLEX TriumphTM X-PET scanner using the NEMA NU-04 standards J. Nucl. Med. 51 1608–15

Prasad R, Ratib O, Zaidi H 2011 NEMA NU-04-based performance characteristics of the LabPET-8™ small animal PET scanner Phys. Med. Biol. 56 6649

Riehakainen L. 2018 Master Thesis, Åbo Akademi University, Turku, Finland.

Rouze N C, Schmand M, Siegel S and Hutchins G D 2004 Design of a small animal PET imaging system with 1 microliter volume resolution IEEE Trans. Nucl. Sci. 51 757–63

Sato K et al 2016 Performance evaluation of the small-animal PET scanner ClairvivoPET using NEMA NU 4-2008 Standards Phys Med Biol 61 696–711

Schafers K P, Reader A J, Kriens M, Knoess C, Schober O and Schafers M 2005 Performance evaluation of the 32-module quadHIDAC small-animal PET scanner J. Nucl. Med. 46 996–1004

Spinks T J , Karia D, Leach M O and Flux G 2014 Quantitative PET and SPECT performance characteristics of the Albira Trimodal pre-clinical tomograph Phys. Med. Biol. 59 715-731

Surti S, Karp J S, Perkins A E, Freifelder R and Muehllehner G 2003 Design evaluation of A-PET: A high sensitivity animal PET camera IEEE Trans. Nucl. Sci. 50 1357–63

Szanda I, Mackewn J, Patay G, Major P, Sunassee K, Mullen G E, Nemeth G, Haemisch Y, Blower P J, Marsden P K 2011 National Electrical Manufacturers Association NU-4 performance evaluation of the PET component of the NanoPET/CT preclinical PET/CT scanner J. Nucl. Med. 52 1741–1747

Tai Y-C, Chatziioannou A, Yang Y, Silverman R W, Meadors K, Siegel S, Newport D, Stickel J R and Cherry S 2003 MicroPET II: design, development and initial performance of an improved microPET scanner for small-animal imaging Phys. Med. Biol. 48 1519–37

Tai Y C, Ruangma A, Rowland D, Siegel S, Newport D F, Chow P L and Laforest R 2005 Performance evaluation of the microPET focus: a third-generation microPET scanner dedicated to animal imaging J. Nucl. Med. 46 455–63

Wang Y, Seidel J, Tsui BM, Vaquero J J and PomperMG 2006 Performance evaluation of the GE healthcare eXplore VISTA dual-ring small-animal PET scanner J. Nucl. Med. 47 1891–900

Wang L, Zhu J, Liang X, Niu M, Wu X, Kao C M, Kim H, Xie Q 2015 Performance evaluation of the Trans-PET® BioCaliburn ® LH system: a large FOV small-animal PET system Phys. Med. Biol. 60 137–150

Xie Q et al 2013 Implementation of LYSO/PSPMT Block Detector With All Digital DAQ System. IEEE Trans. Nucl. Sci. 60 1487–1494

Xie Q, Kao C, Wang X, Guo N, Zhu C, Frisch H, Moses W W, Chen C 2009 Potentials of Digitally Sampling Scintillation Pulses in Timing Determination in PET. IEEE Trans. Nucl. Sci. 56 2607–2613

Xie Q, Kao C M, Hsiau Z, Chen C T 2005 A new approach for pulse processing in positron emission tomography IEEE Trans. Nucl. Sci. 52 988–995

Yamada S, Kubota K, Kubota R, Ido T, Tamahashi N 1995 High accumulation of fluorine-18-fluorodeoxyglucose in turpentine-induced inflammatory tissue. J. Nucl. Med. 36 1301–1306

Yao R, Lecomte R, Crawford E S 2012 Small-Animal PET: What Is It, and Why Do We Need It? J. Nucl. Med. Technol. 40 157–165

Ziemons K et al 2005 The ClearPETTM project: development of a 2nd generation high-performance small animal PET scanner Nucl. Instrum. Methods A 537 307–11